Original Article

Effect of the PEN/C surface layer modification on the microstructure, mechanical and tribological properties of the 30CrMnSiA mild-carbon steel

L.G. Zhurerova[a], B.K. Rakhadilov[b], N.A. Popova[c], M.K. Kylyshkanov[d], V.V. Buranich[e,*], A.D. Pogrebnjak[a,e]

[a] D. Serikbaev East Kazakhstan State Technical University, Ust-Kamenogorsk, Kazakhstan
[b] Sarsen Amanzholov East-Kazakhstan State University, Ust-Kamenogorsk, Kazakhstan
[c] Tomsk State Architecture and Construction University, Tomsk, Russia
[d] Ulba Metallurgical Plant VSC, Ust-Kamenogorsk, Kazakhstan
[e] Sumy State University, 2, Rimsky Korsakov Str., 40007 Sumy, Ukraine

ARTICLE INFO

ABSTRACT

As result of plasma-electrolytic nitrocarburizing 30CrMnSiA carbon steel (ferrite-perlite grade), there was a change in the elemental and phase composition, as well as the surface layer microstructure ($40 \div 45$ microns thick from the surface). A formation of $Me_{23}(CN)_6$ carbonitrides, FeN nitrides, Fe_3C - $(Fe,Cr)_3C$ carbides and an increase in dislocation density within α–phase (tempered martensite crystallites), high-temperature lamellar martensite were observed. As a result of PEN / C exposure for 7 min. at 750 °C there is a reduction of friction coefficient and wear rate, what is connected with finely dispersed secondary phases FeN, $(Fe, Cr)_3C$, $Me_{23}(C, N)_6$ formation. Thus there is an $2,5 \div 3,3$ times increase in hardness of 30CrMnSiA carbon steel samples.

1. Introduction

Electrolyte-plasma processing of metals and alloys is widely used in a semi-industrial scale [1–12]. However, the widespread introduction of all processing types such as electrolyte-plasma oxidation of Ti, Zr, Mg, Al alloys, nitrogen / carbon saturation, thermal quenching and cooling, etc. [13–16], gets difficult due to low repeatability (normally around $95 \div 97,8\%$) whereas the customer requires all 99.99% reproducible processes [17].

Due to its simplicity, plasma electrolytic deposition (PED) processes successfully compete in cost with PVD coatings and electro-galvanizing methods [18–20]. PED can be used to fabricate oxide layers with enhanced mechanical properties during plasma electrolytic oxidation (PEO) or to saturate materials with various alloying elements during plasma electrolytic
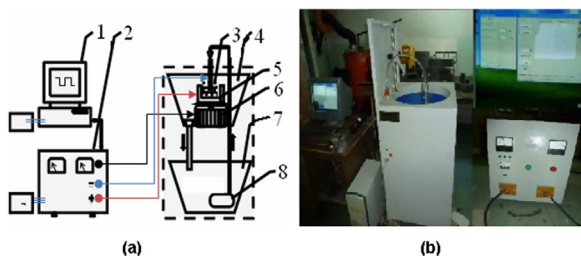
Fig. 1 – Principal scheme (α) and overview (b) of electrolytic plasma treatment (EPT) system:1– computer; 2–power supply; 3– plasma torch; 4– working bath; 5– sample installation part; 6 – stepper motor; 7– electrolyte reservoir; 8 – pump.

saturation (PES). PES processes strongly depends on mean current value (which determines the deposition rate), voltage amplitude of cathode or anode (accordingly to process), working electrolyte temperature and composition. There are also some practical difficulties mentioned precisely in the literature [22–24]. Therefore, mainly the scope of electrolytic plasma treatment (EPT) limited to technologies with reproducibility up to 100%.

EPT processing is one of the most promising and economically feasible techniques. Distinctive features of this method is controllability of the process, wide range of hardening (from several microns to mm), possibility of processing samples, products and working sites of any geometry [14,15]. Treatment of metal samples and products occurs in arc discharge plasma, burning in the active environment of chemical compounds, in particular the chemical-thermal method of the material surface treatment in electrolyte-plasma cathode regime [25–27].

High-energy impact, to which we can add electrolyte-plasma hardening can also be attributed, consists in high-speed heating to temperatures above critical ones by the plasma flow in the local portion of the sample surface layer and its rapid cooling, mainly due to heat conduction to internal volumes of the material, as well as heat transfer from the surface [21].

Thus, the purpose of this work is to study the elemental, phase composition of the surface layers and their microstructure of carbon steel ferrite-perlite class (CrMnSiCFe) and their effect on hardness, wear rate and friction properties as a result of electrolytic plasma treated samples (in solid).

2. Materials and methods

The EPP-processed 30CrMnSiA high strength low alloy (HSLA) steel samples in the as-delivered conditions were used as the material of study (hardened at 880 °C and tempered at 540 °C). Chemical composition of the steel is: C: 0.28-0.35%; Cr: 0.8–1.1%; Mn: 0.8–1.1%; Si: 0.9–1%; P: 0.025%; S: 0.025%, and Fe 9̃6% (30CrMnSiA).

Fig. 1 illustrates a system used for PEN/C processing. A 30CrMnSiA steel specimen to be processed was mounted and clamped on the clamping mechanism. The supply of electrolyte in the dielectric reservoir (15 liters) was provided by a pump designed to work in aggressive environments. As power

supply a powerful rectifier was used, giving a maximum output of 360 V / 60A. The main energy parameters of the plasma jet and movement dynamics of the workpiece were controlled by computer.

PES processing (nitriding, boriding and nitrocarburizing) of 30CrMnSiA structural steel carried by means of the classical technological parameters of plasma-electrolytic modification in two regimes: the temperature was T = 750–950 °C (depending on the type of processing), and the processing duration: 3, 5, 7 min. In the first regime 1:10% of ammonium chloride (NH_4Cl) and 10% of glycerine ($C_3H_5(OH)_3$) electrolyte solution was used and under regime 2: 10% of sodium chloride (NaCl) and 15% of urea (($NH_2)_2CO$) electrolyte accordingly.

Structural-phase examination of 30CrMnSiA steel samples was conducted by the Otto von Guerke University (Magdeburg, Germany). Samples were examined by X-Ray structural analysis using X′PertPRO diffractometer at monochromated CuK_α-radiation, optical microscopy at NEOPHOT 21 and AXIOPHOT-2 machines, transmission electron diffraction microscopy on thin sheet sat JEOL-2100 electron microscope using goniometric devices at raising voltage 100 kV (TGASU, Tomsk, RF).

The microscope column working magnification was 100,000 times. To conduct research with spark cutting, the samples (size $30 \times 30 \times 8 \ mm^3$) were cut into thin sheets (foils) 0.2–0.3 mm thick. Cutted sheets were thinned chemically in the electrolyte of 90% hydrofluoric acid and 10% perhydrol, then by electrolyte in supersaturated solution of phosphoric acid, chrome anhydride at room temperature, operating voltage 20 V and 2–4 A/cm² current density.

The volume fractions of the phases were determined by images confirmed by micro-diffraction patterns and dark-field images taken in the reflexes of corresponding phases. To identify phases there were used the schemes of microdiffraction images calculated from the tabular values of lattice grids.

Energy-dispersive X-ray spectroscopy (EDS) and scanning electron microscopy (SEM) using multifunctional general-purpose scanning electron microscope JEOL JSM-6010/A. In touch scope operated at 20 kV.

Mechanical microhardness tests were carried on the PMT-3 M microhardness tester (St. Petersburg, Russia) after the nitrocarburizing process. A high-temperature tribometer (TNT, CSM Instruments, Switzerland) was used to determine the tribological characteristics. The wear test (wear rate, weight loss) was performed by using pin-on-disk test instrument.

According to the conducted metallographic studies of the 30CrMnSiA steel in the as-delivered conditions [28], it was found that α-phase of varying degrees of doping is the main phase component (matrix) of 30CrMnSiA steel regardless on the sample processing and the place of the study. In its initial state the 30CrMnSiA steel belongs to the ferrite-perlite class containing 6̃5% of perlite grain and 35% of ferrite grain (20% of them are non-fragmented and 15% of fragmented ferrite). It has been established that morphologically α-phase presents in the form of non-fragmented and fragmented ferrite at the boundaries (with an average particle size of 32 nm, volume fraction in the material is 1̃%) and inside (average particle size 4 nm, volume fraction in the material is 0̃,5%) containing carbide particles $M_{23}C_6$; lamellar perlite in the form of
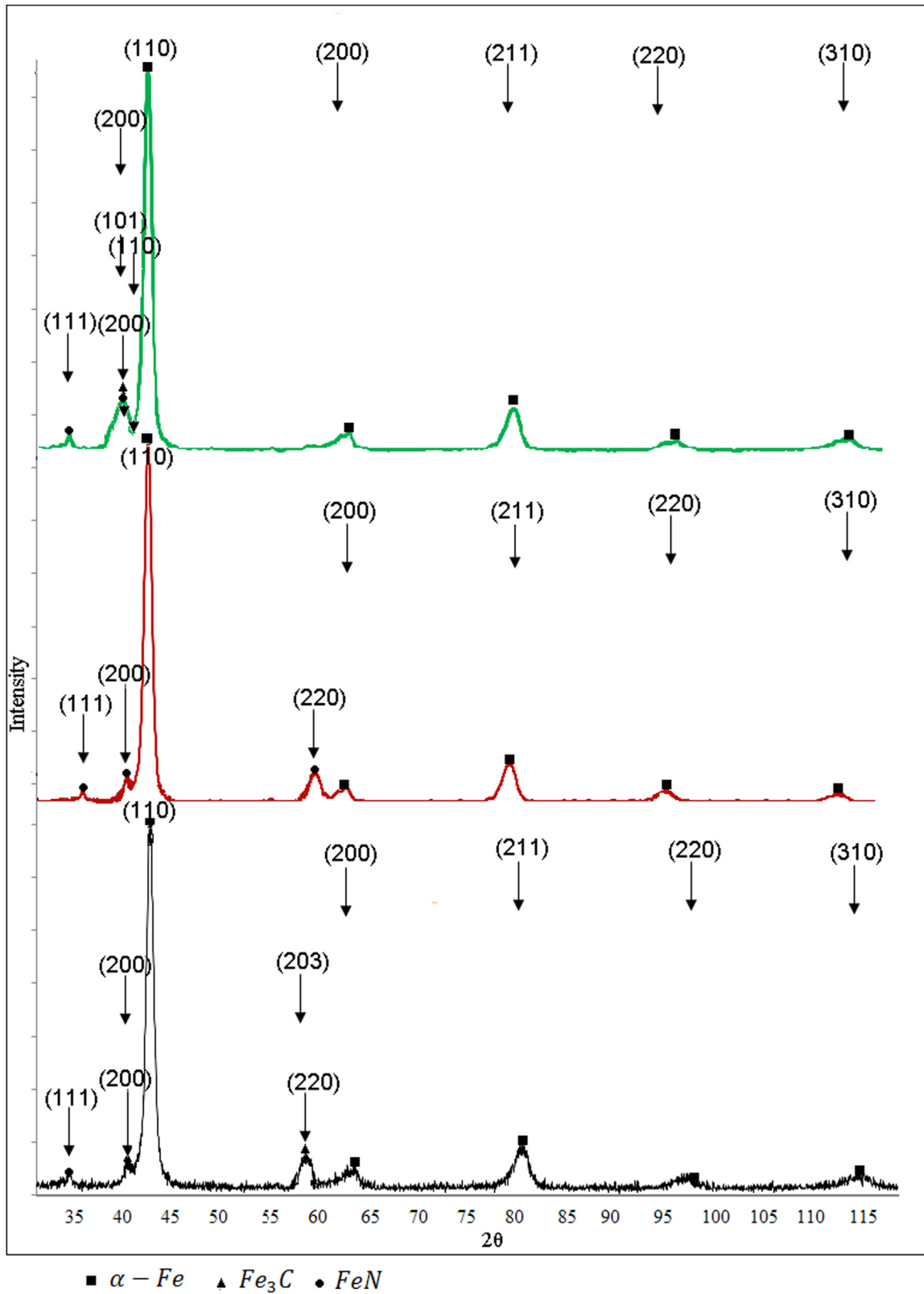
Fig. 2 – XRD patterns of 30CrMnSiA steel sample after high-temperature (T = 750 °C) plasma-electrolyte nitrocarburizing: a) 7 min, b) 5 min, c) 3 min.
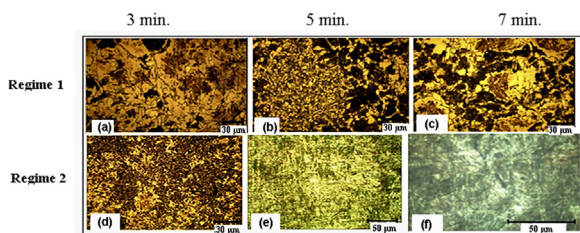
Fig. 3 – SEM microstructures of the modified 30CrMnSiA steel after PEN/C treatment: regime 1 – a) 3 min., b) 5 min., c) 7 min., regime 2 – d) 3 min., e) 5 min., f) 7 min.
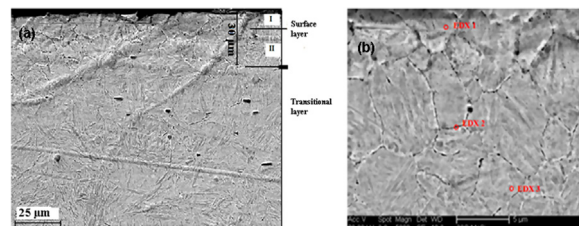

Fig. 4 – Cross-sectional SEM images of nitrocarburized 30CrMnSiA steel structure a) in depth with indexed layer distribution, b) with higher magnification (EDS analysis carried in 3 marked regions).

interchanging parallel plates of ferrite (α-phase) and doped cementite (Cr up to 20%); tempered martensite in the form of mixed structure of lath martensite, low-and high-temperature lamellar martensite.

3. Results and discussion

3.1. Structure and morphology

X-ray diffraction structure investigations of 30CrMnSiA steel carried out after nitrocarburizing has shown at Fig. 2. After modifying in the surface layer nitride FeN, carbide FeC, $(Fe,Cr)_3C$ and carbonitride $M_{23}(C,N)_6$ phases are formed. Martensitic transformations are also noted along the boundaries of which residual austenite is present. Complex carbonitride phases were not detected. Perhaps their volume fraction does not exceed the detection limit of X-ray phase analysis. It is clearly seen how with increasing processing time (3, 5 and 7 min) carbides and nitrides of iron and alloying elements are formed.

Scanning electron microscopy analysis of fragments (Fig. 3) showed that after 30CrMnSiA steel samples electrolytic nitrocarburizing, there is a significant change in the morphology of the surface layer. Enrichment of ferrite with atomic carbon and nitrogen is observed, which contributes to the growth of carbide and nitride particles, as well as martensitic structures in the near-surface modified layer.

Steel nitrocarburizing, as noted above, led to substantial qualitative and quantitative changes in the structure. As the distance from the treated surface changes, such parameters as defect density, organization, size and type, as well as the concentration of alloying elements and impurities. All this eventually led to a change in the phase composition and to the phases formation which inherent in this structural type, as well as their morphology [29,30].

α-phase structure has undergone significant changes. Unlike the initial state, it is a mixture of three morphological components: batch (or rack) tempered low-temperature martensite and high-temperature lamella tempered martensite. Ferrite and perlite grains on nitrocarburized sample surface were not detected by primary analyzes, but they still were observed with TEM studies of thin section (see below).

As we see from the Fig. 3a–c (Regime 1) during plasma electrolytic nitrocarburizing with an increase of the process duration, the dispersion of ferritic particle grains decreases. After 7 min a coarse-grained structure is observed, which is

characterized by stability of carbide and nitride particles with diffusion of implanted atoms, which in turn are responsible for increasing surface hardness and wear resistance.

Sample surface microstructure under 2nd regime (Fig. 3d–f) markedly different from the obtained fragments microstructure obtained under regime 1 conditions. Here, the formation of martensitic phases is visually seen. The layer structure varies with changing the distance from the sample surface.

Fig. 4a, b shows SEM image of surface layer cross-section, obtained with a relatively small magnification. The surface layer is quite clearly divided into two separate zones (I and II), with carbides and carbonitrides distribution. The image shows a well-marked nitrocarburized surface layer, ~30 μm thick. Further, deep into the sample, the transition (intermediate) layer follows, then - the base metal layer (zone). The difference in the structure of the nitrocarburized layer and the changes in its structure with distance from the surface into the sample becomes even more noticeable with a larger magnification (Fig. 4b).

Since the phase composition of the upper-surface is the principal factor that determine mechanical and tribological properties of the modified sample, for its study was carried out Energy-dispersive X-ray spectroscopy (EDS) analysis of the 3 marked regions (Table 1). The increased diffusion of carbon and nitrogen along the grain boundaries in I and II zones due the surface activation by the discharge electric field influence, but this stimulation decreases with increasing depth of analysis.

In the first zone, a weak etching of the grain boundaries is observed, the internal structure of the grains is not clearly expressed. In 2nd zone, the grain boundaries are clearly iden-

Table 1 – Results of elemental composition measurement defined by cross-sectional EDS from 3 different regions of nitrocarburized 30CrMnSiA steel surface.

Element	EDS 1		EDS 2		EDS 3	
	Wt %	At %	Wt %	At %	Wt %	At %
C	22.2	56.6	4.2	16.7	3.9	12.3
O	0.0	0.0	0.0	0.0	10.9	26.0
N	0.6	0.3	0.9	0.8	0.9	1.6
Si	1.2	1.3	1.4	2.4	3.4	4.7
Cr	1.1	0.7	1.3	1.2	2.3	1.7
Fe	74.9	41.2	92.1	78.9	77.4	52.9
Mn	0.0	0.0	0.0	0.0	1.1	0.8
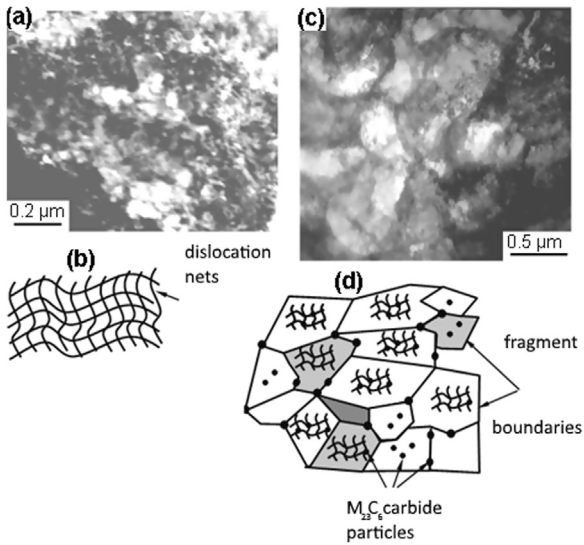
Fig. 5 – Non-fragmented and fragmented ferrite in the initial state of 30CrMnSiA steel.
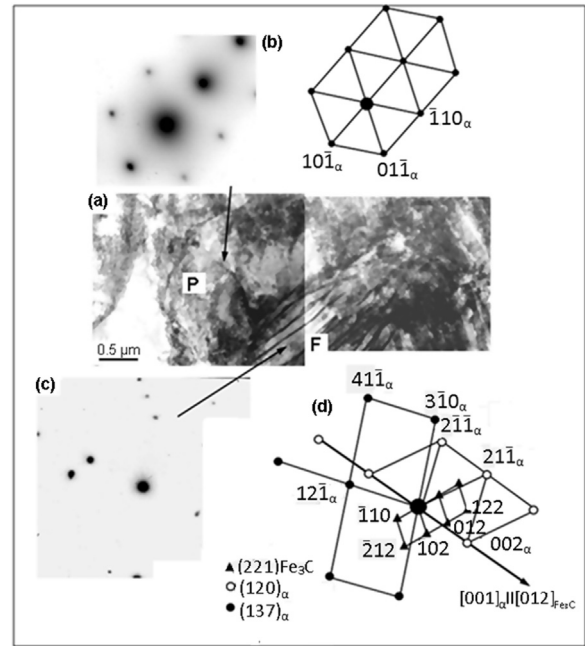

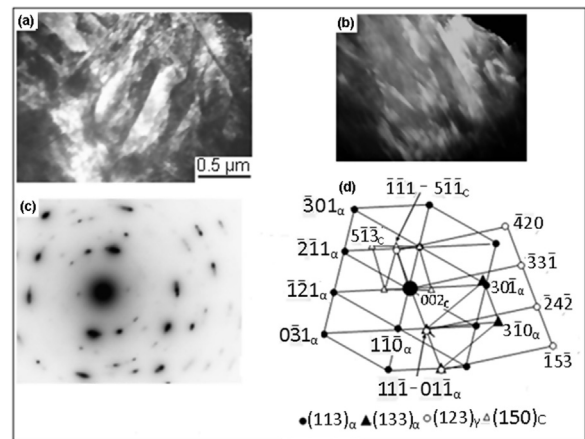Fig. 6 – TEM image of 30CrMnSiA steel microstructure in its initial state.

Fig. 7 – TEM image of tempered lath martensite. Separating of γ-phase along the boundaries of the laths and $M_{23}(C,N)_6$ carbonitride particles on the dislocations inside the laths. 30CrMnSiA steel is after nitrocarburizing. Surface of the sample: a — bright field image; b – dark field image; c —microdiffraction image; d –identified scheme.

tified, and a rather well-defined structure inside the grain is present. This is especially clearly seen on thin sections, where the etching was carried out to identify not only the grain boundaries, but also to reveal the internal structure of the grains (Fig. 4a). At transition zone, which follows the nitrocarburized layer, the clearly identified grain boundaries, there is also a fairly well-defined structure inside the grains (Fig. 4b).

Grain size increases as the material moves deeper into the material: the average grain size is minimal on the surface of the processed sample, then it quickly increases to a depth of $\tilde{2}$00 μm (at large distances from the surface the study was not conducted). Note that different grain sizes from 10 nm to μm increases the strength characteristics (properties) of 30CrMnSiA structural steel [23,24].

Fig. 5 illustrates examples of non-fragmented ferrite 5a and its schemes 5b; fragmented ferrite 5c and its schemes 5d in the initial state in 30CrMnSiA steel.

Fig. 6 illustrates electron-microscopy image of 30CrMnSiA structure in its initial state: a – bright field image (F – ferrite grain, P – lamellar perlite grain); b – microdiffraction image and its indicated diagram taken from the ferrite grain. There are some reflexes related to $(111)_\alpha$ flat area; c - microdiffraction image and d- it is indicated diagram, taken from the grains of perlite, there are also reflexes related to flat area (120) and (137) α-phase and (221) of cementite Fe_3C. The arrow points coinciding directions of α-phase [001] and cementite [0$\bar{1}$2], i.e. $[001]_\alpha \: II \: [0\bar{1}2] \: Fe_3C$, the relation: $(120)_\alpha II (221)_{Fe_3C}$ (Bagaryatsky ratio).

Fig. 7 illustrates Electron-microscopy image of tempered lath martensite. It is a process of separating of γ-phase along the boundaries of the laths and presenting of $M_{23}(C,N)_6$ carbonitride particles on the dislocations inside of the laths. 30CrMnSiA steel is shown after nitrocarburizing. Surface of the sample is as follows: a—bright field image; b—dark field image; c—microdiffraction image; d—its indicated scheme. There are also reflexes belonging to the flat areas (113) and

(133) α- phase, (123) γ- phase and (150) of $M_{23}(C,N)_6$, carbonitride marked as "C" at scheme.

The α-phase structure was significantly changed. In contrast to its initial state, it presents a mixture of three morphological components: lath tempered martensite (Fig. 7), lamellar tempered low-temperature martensite (Fig. 8c) and lamellar tempered high-temperature martensite (Fig. 8b). There are no ferrite and perlite grains on the EPP-processed sample surface. As it was mentioned above, lath martensite is a structural formation, which featured with joined equally

Table 2 – Morphological components of α-phase in 30CrMnSiA steel after nitrocarburizing and quantitative share of γ-phase there (Electron microscopy data).

| Morphological components of steel matrix		Volume share in steel matrix P_V, (%)	Share of retained austenite in crystals α-phase, δ,(%)
Sample surface			
Tempered martensite	Lath martensite	30%	1.5
	Lamellar low-temperature martensite	20%	1.7
	Lamellar high-temperature martensite	50%	4.0
Inside of material		100%	2.6
50 μm from the sample surface			
Tempered martensite	Lath martensite	55%	1.3
	Lamellar low-temperature martensite	20%	4.7
	Lamellar high-temperature martensite	25%	6.0
Inside of material		100%	3.2
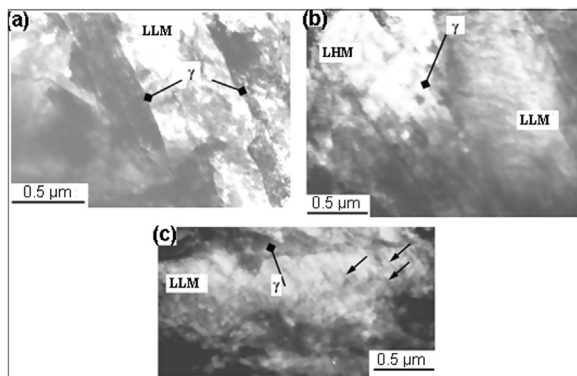
Fig. 8 – Microstructure of the 30CrMnSiA steel sample surface after nitrocarburizing. LLM – lamellar low-temperature martensite; LHM – high-temperature martensite. Retained austenite (γ) at the boundaries of the lamellar (α) as twin-type colonies (b) and small regions (c). Cementite particles (c) indicated by arrows.
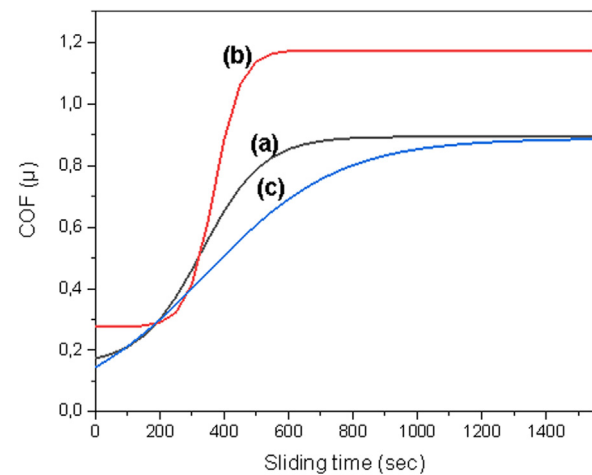

Fig. 9 – Coefficient of Friction (COF) against Sliding time dependence of the 30CrMnSiA steel samples: a) Initial, b) Nitriding, c) Nitrocarburizing.

oriented crystals of martensite - laths which form individual packages. The volume fraction of the martensite in steel matrix is $\bar{3}0\%$ of the volume of steel matrix, Table 2. Lamellar martensite is like single martensite crystals (LLM), which are not grouped into packages [31]. This is a morphological component of the steel matrix and makes $\bar{2}0\%$ of the volume of the steel matrix, Table 2. Lamellar high-temperature martensite (LHM) is some structurless regions without clearly defined boundaries. This is the main morphological component of the steel matrix which makes about 50% of the volume of steel matrix, Table 2.

The γ-phase presents in the form of retained austenite and it is located either as interlayers along the boundaries of martensite laths (Fig. 7) and lamellars (Fig. 8a) or inside of the martensite lamellars in the form of twin-type colonies (Fig. 8b), or small regions (Fig. 8c). Table 2 provides data on volume fraction of γ - phase in various morphological components of α - phase.

Nitrocarburizing resulted in carbide subsystem changes of steel-cementite that presents inside the crystals of tempered martensite (Fig. 6c). The particles are acicular form with different size and distribution density in any morpho-

logical components of α-phase. However, the volume fraction of cementite in each morphological component of the α-phase does not exceed 0.4-0.5% from total volume of material.

Such carbonitrides as $M_2C_{0.61}N_{0.39}$, $M_4(C,N)$, $M_7(C,N)_3$ and $M_{23}(C,N)_6$ are generated on the sample surface in all morphological components of α-phase after nitrocarburizing.

Steel nitrocarburizing caused a formation of two more carbonitride types: $M_4(C, N)$ and $M_7(C, N)_3$ on the sample surface as it was noted above. It was found that some nanoparticles ($\bar{5}$-8 nm) of carbonitride $M_4(C,N)$ are formed on the interfacial surfaces "Carbonitride $M_7(C,N)_3$ - α-phase" with average size of $\bar{0}.2\,\mu m$.

A decrease of dislocations density along the sample surface (Table 3) responds to indicate the manifestation of diffuse shear deformation during saturation process that also affects hardening of the material.

3.2. Tribological and mechanical properties

At Figs. 9–11 (Table 4) the experimental data from tribological tests on modified 30CrMnSiA steel samples by different

Table 3 – Morphological components of α-phase in 30CrMnSiA steel after nitrocarburizing and quantitative characteristics of dislocation structure (Electron microscopy data).

Morphological components of steel matrix		Volume share in steel matrix P_V, (%)	Dislocation density, $\rho \times 10^{-10}$, (cm^{-2})	Excess of dislocation density, $\rho \times 10^{-10}$, (cm^{-2})
Sample surface				
Tempered martensite	Lath martensite	30%	4.4	0
	Lamellar low-temperature martensite	20%	3.9	0
	Lamellar high-temperature martensite	50%	3.5	0
Inside of material			3.9	0
50 μm from the sample surface				
Tempered martensite	Lath martensite	55%	7.6	2.9
	Lamellar low-temperature martensite	20%	4.1	4.1
	Lamellar high-temperature martensite	25%	3.2	1.2
Inside of material			5.8	2.7

Table 4 – Results of tribological testing.

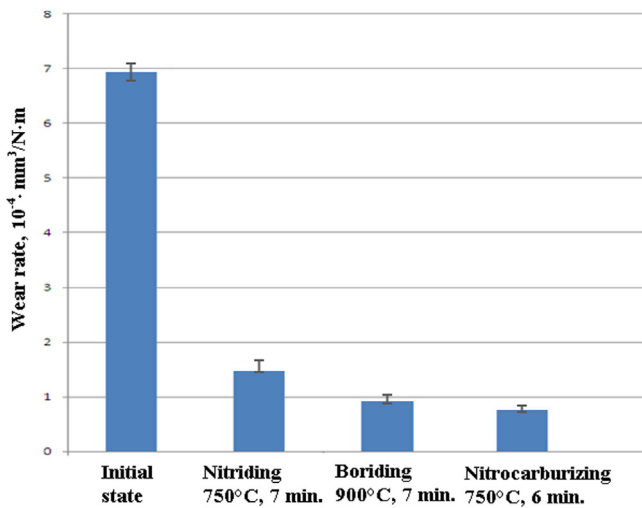| №	Type of electrolytic treatment	Wear rate [(mm^2/N)/mm],	Coefficient of friction, μ
1	Initial state	0,00071	0,9
2	Nitriding 750 °C, 7 minutes	0,000164	1,4
3	Boriding 900 °C, 7 minutes	0,0001	0,6
4	Nitrocarburizing 750 °C, 6 minutes	0,00008106	0,8

Fig. 10 – Wear rate behavior (diagram) of 30CrMnSiA steel samples under different plasma electrolytic treatment.
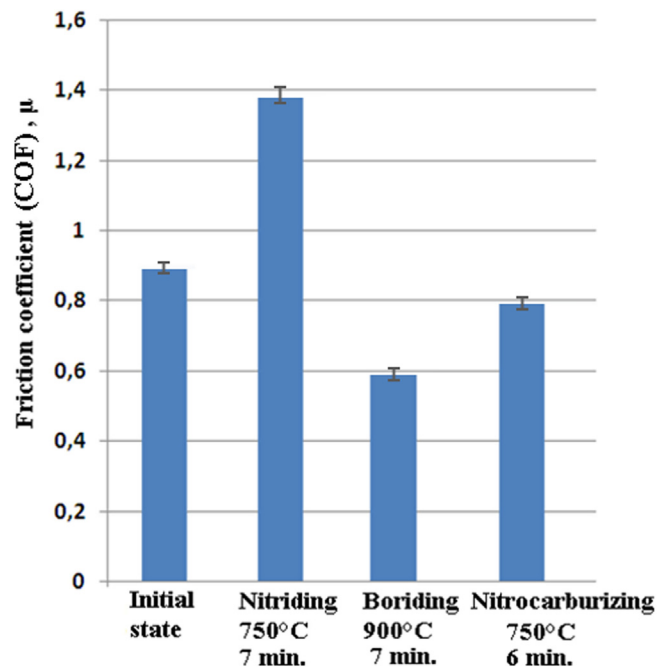

Fig. 11 – Friction coefficient behavior (diagram) of 30CrMnSiA steel samples under different plasma electrolytic treatment.

types of electrolytic treatment and dependences of the wear rate (mm^3/N × mm), coefficient of friction (COF) are presented.

According to the Table 4 wear rate of the 30CrMnSiA steel samples compared to the initial state varies with different dynamics. A noticeable decrease in the wear rate can be seen for samples obtained after nitrocarburizing at T = 750 °C for 6 min at 8.7 times, nitriding at T = 850 °C for 7 min at 4.3 times, boriding at T = 950 °C during 7 min at 7.1 times accordingly. According to Table 4, we plotted the experimental data on wear resistance (Fig. 10) and the friction coefficient (Fig. 11) of all

treated 30CrMnSiA steel samples. Fig. 12 shows micrographs of the 30CrMnSiA steel upper-surface after the tribological tests. Based on the nature of the surface damage trace, it can be concluded that samples obtained during nitrocarburizing treatment acquire a higher wear resistance.
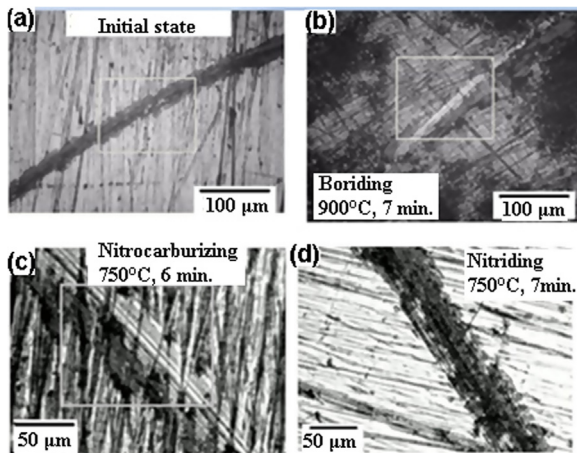
Fig. 12 – Micrographs of the 30CrMnSiA steel surface after the tribological tests.

The results of experimental work on the modified surface microhardness determination carried on the microsection of 30CrMnSiA steel, after the PEN/C process has shown at Figs. 13 and 14.

From the obtained experimental data about the modified surface layers microhardness determination, an already established regularity can be observed: with increasing hardness of surface, the degree of doping of the material also increases [32], on the basis of which lies the choice of the optimal mode. However, in world practice [33–35] the opposite concept also exists: not all wear-resistant materials have a high surface hardness [36,37]. Nevertheless, according to our research on the microhardness and wear resistance determination, the following regularities were established: with an increase in the wear resistance of the 30CrMnSiA steel samples surface during plasma electrolytic saturation (PES): nitriding, boriding and nitrocarburizing a significant increase in microhardness has been observed. Samples processed in nitrogen-containing electrolytes showed increase in microhardness by an order of magnitude, which is most likely due to the formation of finely dispersed nitrides on modified lay-

ers. The maximum microhardness value is a nitrocarburized 30CrMnSiA steel sample at regime 1 which is equal to 8.9 GPa, and the surface microhardness after processing at regime 2 is 3.2 GPa (Figs. 13 and 14), which corresponds to the minimum microhardness value.

Analyzing the experimental data, it can be seen that with hardness increase (Fig. 13), the resistance to wear (Fig. 10) also increases, however, this pattern does not appear in all cases during the nitrocarburizing process [30].

All changes in mechanical (hardness) and tribological (friction coefficient, wear rate) properties are associated within the formation of the secondary phases: nitrides, carbides, carbonitrides, iron borides and alloying elements. On the other hand, changing the temperature, electrolyte composition, current and potential (actual processing parameters) can also affect the microstructure, uniformity and degree of alloying of the material, which consequently contributes to the steel samples modification.

4.   Conclusion

1) Samples obtained during plasma-electrolytic processing of 30CrMnSiA mild-carbon steel surface demonstrate 2.5 times increase in microhardness and 4 times increase in wear resistance;
2) Found out that the ferrite-pearlite structure of the steel matrix is modified according to the method of electrolytic saturation (PES):
3) Upon nitrogen, boron and carbon saturation for 3, 5, 7 min and working temperature T = 750–950 °C followed by quenching in electrolyte, a modified layer (average thickness 30 μm) is formed, that includes nitride FeN, carbide FeC, (Fe, Cr)$_3$C and complex carbonitride phases.
4) Revealed, that hardening of 30CrMnSiA structural steel occurs in low-temperature plasma conditions, due to the formation of carbides, carbonitrides, and alloying elements, that enhance performance at effective surface modification until the heat affected zone (hardening depth $\bar{4}$5 μm).
5) Upon nitrocarburizing (regime 1) at 750 °C, 3–7 minutes followed by quenching in the electrolyte containing an
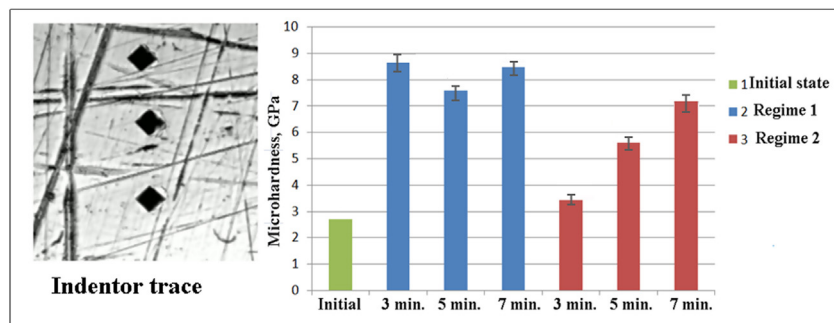

Fig. 13 – Diagram of the surface microhardness after nitrocarburizing process in electrolyte plasma against time and working solution type (green – Initial state, blue – Regime 1, T = 750 °C (10% NH$_4$Cl + 10% C$_3$H$_5$(OH)$_3$), red – Regime 2 T = 750 °C (10% NaCl + 15% (NH$_2$)$_2$CO) (For interpretation of the references to colour in this figure legend, the reader is referred to the web version of this article).

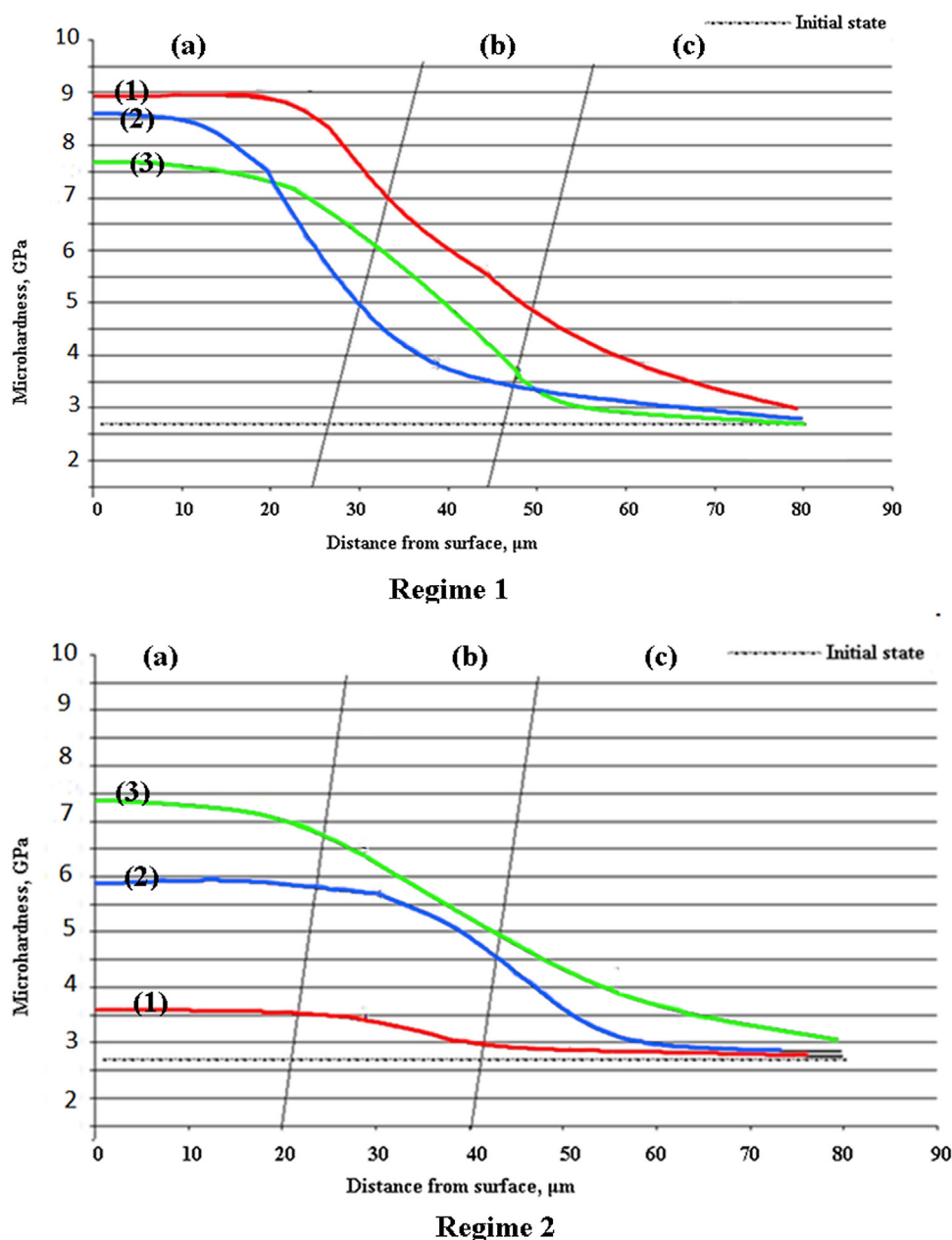**Fig. 14 – The microhardness distribution along the cross-section depth of 30CrMnSiA steel after nitrocarburizing T=750 °C, 1–3 min, 2–5 min, 3–7 min, a −α-Fe + FeC + (Fe, Cr)$_3$C + M$_{23}$(C, N)$_6$; b − M + γ-Fe; b − α-Fe.**

aqueous solution of 10% (NH$_4$Cl) +10% (NaCl) and 15% ((NH$_2$)$_2$CO), surface microhardness increases by 3,3 times, wear resistance increases by 8.7 times depending on the processing type of the initial sample.

Conflicts of interest

The authors declare no conflicts of interest.

Acknowledgments

REFERENCES

[1] Markov GA, Tatarchuk VV, Mironova MK. Microarc oxidation of aluminium in the concentrated sulfuric acid. Ser. Khim. Nauk. Novosibirsk 1983 (in Russian).

[2] Snezhko LA, Beskrovnyj YuM, Nevkrytyj VI, Tchernenko VI. Pulsed mode for producing silicate coatings in a spark discharge. Zashch, Met 1980 (in Russian).

[3] Snezhko LA, Tchernenko VI. Energy parameters of the process of obtaining silicate coatings on aluminum in the

spark discharge mode. Electron Obrab. Mater 1983 (in Russian).

[4] Fyedorov VA, Belozerov VV, Velikosel'skaya ND, Bulchev SI. Composition and structure of the hardened aluminum alloys surface layer obtained by microarc oxidation. Fiz. Khim. Obrab. Materialov 1988;4:92 (in Russian).

[5] Ditrich KH, Krysmann W, Kurze P, Schneider HG. Process characteristics and parameters of anodic oxidation by spark discharge. Cryst Res Technol 1984;19(1):93.

[6] Pogrebnjak AD, Kul'ment'eva OP, Kobzev AP, Tyurin YuN, Golovenko SI, Boiko AG. Mass transfer and doping during electrolyte-plasma treatment of cast iron. Tech Phys Lett 2003;29:312–5, http://dx.doi.org/10.1134/1.1573301.

[7] Belkin PN, Kusmanov SA, Dyakov IG, Komissarova MR, Parfenyuk VI. Anode plasma electrolytic carburizing of commercial pure titanium. Surf Coat Technol 2016;307:1303, http://dx.doi.org/10.1016/j.surfcoat.2016.04.057.

[8] Belkin PN, Kusmanov SA. Plasma electrolytic nitriding of steels. J. Surf. Invest.: X-Ray, Synchrotron Neutron Tech 2017;11:767.

[9] Andrei VA, Malinovschi V, Radulescu C, Ionita I, Torok G, Coaca E, et al. Applications of plasma electrolytic saturation technique in the field of nuclear materials. Journal Of Science And Arts 2019;19:185.

[10] Noori SM, Dehghanian C. Characterization of nitrocarburized coating by plasma electrolytic saturation. Acta Metall. Slovaca 2018;24:20, http://dx.doi.org/10.12776/ams.v24i1.957.

[11] Clyne TW, Troughton SC. A review of recent work on discharge characteristics during plasma electrolytic oxidation of various metals. Int Mater Rev 2018;64:127, http://dx.doi.org/10.1080/09506608.2018.1466492.

[12] Hryniewicz T. Plasma electrolytic oxidation of metals and alloys. Metals 2018;8:1058, http://dx.doi.org/10.3390/met8121058.

[13] Sundararajan G, Krishna LR. The tribological performance of ultra-hard ceramic composite coatings obtained through microarc oxidation. Surf Coat Technol 2003;167(269), http://dx.doi.org/10.1016/S0257-8972(02)00646-1.

[14] Yerokhin AL, Voevodin AA, Lyubimov VV. Plasma electrolytic fabrication of oxide ceramic surface layers for tribotechnical purposes on aluminium alloys. Surf Coat Technol 1998;110:140, http://dx.doi.org/10.1016/S0257-8972(98)00694-X.

[15] Yerokhin AL, Snizhko LO, Gurevina NL, Matthews A. Discharge characterization in plasma electrolytic oxidation of aluminium. J Phys D: Appl Phys 2003;36:2110, http://dx.doi.org/10.1088/0022-3727/36/17/314.

[16] Yerokhin AL, Nie X, Leyland A, Matthews A, Dowey SJ. Plasma electrolysis for surface engineering. Surf. and Coat. Tech 1999;122:73–93, http://dx.doi.org/10.1016/S0257-8972(99)00441-7.

[17] Tyurin YN, Pogrebnjak AD. Electric heating using a liquid electrode. Surf. And Coat. Tech 2001;142–144:293–9, http://dx.doi.org/10.1016/S0257-8972(01)01207-5.

[18] Li HX, Rudnev VS, Zheng XH. Characterization of Al_2O_3 ceramic coatings on 6063 aluminum alloy prepared in borate electrolytes by micro-arc oxidation. J Alloys Compd 2008;462:99–102, http://dx.doi.org/10.1016/j.jallcom.2007.08.046.

[19] Snizhko LO, Yerokhin AL, Pilkington A. Anodic processes in plasma electrolytic oxidation of aluminium in alkaline solutions. Electrochim. Acta 2004;49:2085, http://dx.doi.org/10.1016/j.electacta.2003.11.027.

[20] Cai QZ, Wang LS, Wei BK, Liu QX. Electrochemical performance of microarc oxidation films formed on AZ91D magnesium alloy in silicate and phosphate electrolytes. Surf Coat Technol 2006;200:3727, http://dx.doi.org/10.1016/j.surfcoat.2005.05.039.

[21] Duradji VN. Chemical heat treatment of metals with heating in electrolytic plasma. Actual Conference 2010;6(69):59–61 (in Russian).

[22] Belkin PN, Ganchar VI, Tovarkov AK. Investigation of steam film conductivity under anodic electrolytic heating. J Eng Phys Thermophys 1986;51:154–5 (in Russian).

[23] Belkin PN, Ganchar VI. Volt-temperature and volt-ampere characteristics of the anodic process of electrolytic heating. Electr. Obrab. Mat 1989;5:59–62 (in Russian).

[24] Gordienko P, Zhevtun I, Dostovalov A. Composition and structure of carbon-rich local sections formed on titanium alloys in electrolytes. Russian Engineering Research 2012;32:158–61, http://dx.doi.org/10.3103/S1068798X12020104.

[25] Tyurin YuN, Pogrebnjak AD. Specific features of electrolytic-plasma quenching. Tech.Phys 2002;47(11):1463–4, http://dx.doi.org/10.1134/1.1522119.

[26] Pogrebnjak AD, Tyurin YN. Modification of material properties and coating deposition using plasma jets. Tech. Phys. (Rus.) 2004;74:109–12, http://dx.doi.org/10.3367/UFNr.0175.200505e.0515.

[27] Gupta P, Tenhundfeld G. Synthesis and characterization of hard metal coatings by electro-plasma technology. Plating Surf. Finish 2005;92:48, http://dx.doi.org/10.1016/j.surfcoat.2005.08.030.

[28] Skakov M, Zhurerova L, Scheffler M. Influence of regimes electrolyte-plasma processing on phase structure and hardening of steel 30CrMnSi. Adv Mater Res 2013;601:79–83, http://dx.doi.org/10.4028/www.scientific.net/AMR.601.79.

[29] Skakov M, Zhurerova L, Scheffler M. Way of hardening surface coating of details from steel 30CrMnSi in electrolytic plasma. Key Eng Mater 2013;531–532:178–81, http://dx.doi.org/10.4028/www.scientific.net/KEM.531-532.178.

[30] Wang B, Xue W, Wu J, Jin X, Hua M, Zhenglong W. Characterization of surface hardened layers on Q235 low-carbon steel treated by plasma electrolytic borocarburizing. J Alloy Compd 2013;578:162–9, http://dx.doi.org/10.1016/j.jallcom.2013.04.153.

[31] Kozlov EV, Gromov VY, Kovalenko VV. Gradient structures in perlite steel. Phys Mezomech Novokuznetsk 2004;220 (in Russian).

[32] Ivanov YuF, Kozlov EV. Volume and surface hardening of structural steel – morphological analysis of the structure. News of high schools. Physics 2002;3:5–23.

[33] Tang L, Yan MF. Microstructure and mechanical properties of surface layers of 30CrMnSiA steel plasma nitrocarburized with rare earth addition. J Rare Earth 2012;30:1281–6, http://dx.doi.org/10.1016/S1002-0721(12)60221-X.

[34] Tang NL, Yan MF. Influence of plasma nitriding on the microstructure, wear, and corrosion properties of quenched 30CrMnSiA steel. JMEP 2013;22(7):2121–9, http://dx.doi.org/10.1007/s11665-013-0488-0.

[35] Pogrebnjak AD, Lozovan AA, Kirik GV. Structure and properties of nanocomposite, hybrid and polymer coatings. Moscow: Publ. URSS; 2011. p. 344.

[36] Pogrebnjak AD, Kaverina A, Kylyshkanov MK. Electrolytic plasma processing for plating coatings and treating metals and alloys. Prot Met Phys Chem 2014;50:72–87.

[37] Pogrebnyak AD, Kylyshkanov MK, Tyurin YN, Kaverina A, Yakushchenko IV, Borisenko AA, et al. Properties and structure of oxidized coatings deposited onto Al-Cu and Al-Mg alloys. Tech Phys 2012;57:840–8, http://dx.doi.org/10.1134/S1063784212060217.